Interfacial Growth of Metal Organic Framework/Graphite Oxide Composites through Pickering Emulsion and Their CO_2 Capture Performance in the Presence of Humidity

Zijun Bian,[†] Jian Xu,[‡] Shenping Zhang,[†] Xiaomin Zhu,[†] Honglai Liu,[†] and Jun Hu*,[†]

[†]State Key Laboratory of Chemical Engineering and Department of Chemistry, East China University of Science and Technology, Shanghai 200237, China

[‡]Shanghai Institute of Measurement and Testing Technology, 1500 Zhang Heng Road, Shanghai 201203, China

Ⓢ *Supporting Information*

ABSTRACT: We proposed an in situ interfacial growth method induced by the Pickering emulsion strategy to produce metal organic framework (MOF)/graphite oxide (GO) composites of $Cu_3(BTC)_2$/GO, in which GO was demonstrated to be a promising stabilizer for producing the Pickering emulsion and provided a large interfacial area for the in situ growth of $Cu_3(BTC)_2$ nanoparticles. When $Cu_3(BTC)_2$/GO composites were used as adsorbents for CO_2 capture from the simulated humid flue gas, they showed both significantly improved thermodynamic and dynamic properties. Because most of the H_2O molecules were adsorbed on the highly exfoliated GO sheets in $Cu_3(BTC)_2$/GO-m, CO_2 uptake reached 3.30 mmol/g after exposure to the simulated flue gas for 60 min and remained unchanged for up to 120 min. This highlighted its potential application for real CO_2 capture. More importantly, the in situ interfacial growth of nanoparticles induced by Pickering emulsions would be a promising strategy for designing and fabricating nanocomposites.

INTRODUCTION

The adsorption technique has been proven to be one of the most promising techniques to reduce CO_2 emissions against fossil fuel combustion.[1,2] An important issue for improving the efficiency of the adsorption technique is to seek novel adsorbents with outstanding CO_2 adsorption performance.[3] Many adsorbents, such as zeolites,[4] activated carbons,[5] and metal organic frameworks (MOFs),[6] have achieved great progress. However, all of them meet a great challenge in the real CO_2 capture processes in that their CO_2 adsorption efficiency decreases significantly because the flue gas is always present with humidity, and they inherently show better affinity for the polar H_2O molecule.[7−10]

MOFs, owing to the diversity of chemistry, the network geometry, and the porosity, have sparked research interest in gas storage and separation.[11,12] However, their stability, especially with respect to humidity, limits their further applications.[13] One of the most promising solutions is to produce MOF-based composites, such as alumina,[14] silica,[15] functionalized self-assembled monolayers,[16,17] functionalized graphite,[18] polymer nanoparticles,[19] carbon nanotubes,[20] and graphite oxides (GO),[21,22] because the composites can provide various desirable properties to meet multiple functional demands as well as good mechanical structures and stabilities. It was found that the oxygen-containing functional groups (hydroxyl, carboxyl, epoxy, and ketone) of GO were able to coordinate to the metallic centers of the MOFs and thus allowed the growth of MOF crystals on the GO sheets.[23,24] Synergistic effects of the GO substrate on the porosity and the chemistry of MOFs resulted in a significant improvement in the adsorption of small gas molecules under ambient conditions, such as H_2,[25] NH_3,[26] and CO_2.[22,27,28] However, the morphologies of most reported MOF/GO composites were usually a huge monolith or the closely packed layered block, which significantly limited the deserved advantages of graphene sheets.[29] Although there are already some successful approaches for the exfoliation of GO in solution,[30] the fabrication of composites with highly dispersed GO sheets remains a great challenge.[31]

With oxygen-containing groups on the two-dimensional graphene sheets, the increased hydrophilicity of GO causes it to be easily dispersed in the interface of the water−oil binary system.[32−34] These properties makes great sense for producing the Pickering emulsion.[35] Stabilized by the self-assembly of amphiphilic nanoparticles such as silica, proteins, metal oxides, and carbon black at a liquid−liquid interface, Pickering

emulsions have been widely used in various fields.[36−38] Recently, GO has also been reported to be a successful stabilizer for Pickering emulsions in which GO sheets were highly exfoliated and dispersed at the surface of the Pickering emulsion droplets.[39] Huang et al.[33] studied the activity of GO at air−water, liquid−liquid, and liquid−solid interfaces and found that GO can act as a molecular amphiphile as well as a colloidal surfactant. In fact, the large liquid−liquid interface of the Pickering emulsion stabilized by the nanoparticles would provide a great space for the in situ interfacial growth of new types of nanoparticles to produce novel composites.[40] The significance of the Pickering emulsion method for the fabrication of GO-based composites is attracting more and more attention. Mohsen et al.[41] synthesized nanocomposites by Pickering emulsion polymerization at the liquid−liquid interface with a system of poly(methyl methacrylate) (PMMA)-GO. Tang et al.[42] fabricated gold nanoparticle/graphene oxide hybrides (AuNP/GO) and prepared AuNP/GO supported polystyrene (PS) microspheres (AuNP/GO@PS) by polymerizing the Pickering emulsion. AuNP/GO@PS showed good catalytic performance for the reduction of 4-nitrophenol. However, for most reported GO-based composites produced by the Pickering emulsion method, nanoparticles should be ready-made or should even be surface-modified to render them compatible with GO, which is usually complicated and elaborate.

Herein, we reported an in situ interfacial growth strategy for fabricating MOF/GO composites induced by the Pickering emulsion. $Cu_3(BTC)_2$ was selected as a representation of MOFs because it is the most studied MOF and shows very good CO_2 adsorption capacity. GO was expected to bring about three aspect advantages. First, it can be a promising stabilizer for producing the Pickering emulsion and hence for providing a large interfacial area for the interfacial growth of $Cu_3(BTC)_2$ nanoparticles to produce the $Cu_3(BTC)_2$/GO composites. Second, it can significantly modify the morphology and surface porosity of $Cu_3(BTC)_2$ nanoparticles and hence improve their CO_2 adsorption performance in both thermodynamic and dynamic ways. Third, the highly dispersed GO sheets can enhance the surface water-resistance of the composites and hinder the entrance of water molecules into $Cu_3(BTC)_2$ particles and hence improve CO_2 adsorption properties in the presence of humidity. Bu varying the GO content, the stability of $Cu_3(BTC)_2$/GO Pickering emulsions, the structure of $Cu_3(BTC)_2$/GO composites, and their CO_2 adsorption performance from the simulated humid flue gas were investigated.

■ EXPERIMENTAL SECTION

Materials. Nature graphite flakes (supplied by Huadong Graphite Processing Factory) were used for the GO synthesis. 1,3,5-Benzenetricarboxylic acid (H_3BTC), $NaNO_3$, $Cu(NO_3)_2$, H_2SO_4, $KMnO_4$, and H_2O_2 were purchased from Shanghai Ling Feng Chemical Reagent Co., Ltd. All reagents were reagent grade and used as purchased without further purification.

Preparation of GO Solution. GO was synthesized using a modified Hummers and Offeman's method.[43] In a typical synthesis, graphite (0.5 g), $NaNO_3$ (0.5 g), and H_2SO_4 (23 mL) were mixed together under stirring in an ice bath for 15 min. Then $KMnO_4$ (4 g) was slowly added, and the solution was transferred to a 35 °C bath under stirring. After about 2 h, a thick green paste was produced. Then water (40 mL) was added very slowly under stirring while the temperature reached 90 °C. After 1 h, water (100 mL) was added. Finally, H_2O_2 (30%, 3 mL) was added very slowly, turning the color of

the solution from dark brown to pale yellowish brown. The warm solution was then filtered and washed with water. The final product of GO was dispersed in water (2 mg/mL) for the preparation of $Cu_3(BTC)_2$/GO composites.

Preparation of $Cu_3(BTC)_2$/GO Composites. For the Pickering emulsion system, as illustrated in Scheme 1, the oil phase consisted of

Scheme 1. Schematic Illustration of the Synthesis Approach for $Cu_3(BTC)_2$/GO
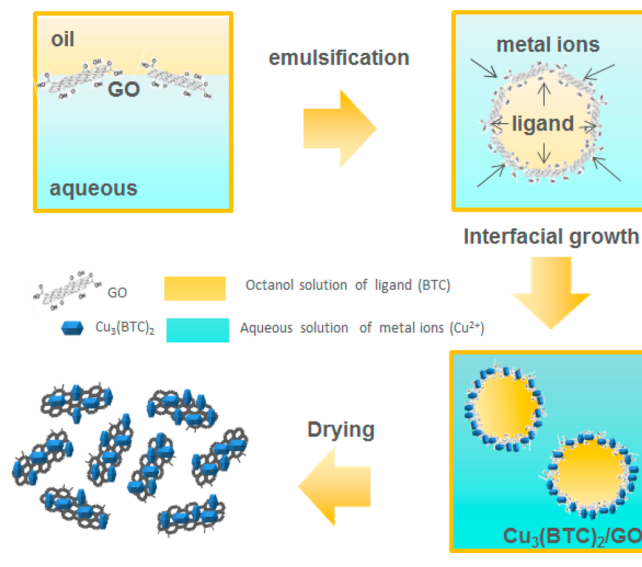
n-octanol (5 mL) with H_3BTC (0.06 g) dissolved, and the water phase consisted of water (5 mL) with $Cu(NO_3)_2$ (0.06 g) dissolved and a GO aqueous suspension. The oil solution and aqueous solution were added to a 25 mL beaker and emulsified with a B25 emulsifier (B.R.T Co., Ltd.) at a speed of 10 000 rpm for 5 min. Then the mixture was heated to 60 °C and maintained for 60 min to produce $Cu_3(BTC)_2$ at the interface of GO Pickering emulsion droplets. With different added amounts of the GO aqueous suspension (2 mg/mL) of 2, 5, and 10 mL, the products were denoted as $Cu_3(BTC)_2$/GO-l, $Cu_3(BTC)_2$/GO-m, and $Cu_3(BTC)_2$/GO-h, respectively. Pristine MOF of $Cu_3(BTC)_2$ was also synthesized at 60 °C for comparison. All of the samples were dried at 60 °C under vacuum for 24 h before characterization.

For comparison, the mixtures of preformed $Cu_3(BTC)_2$ and GO by simply mixing and by growing $Cu_3(BTC)_2$ in the bulk GO aqueous suspension without emulsification were also prepared. For the former, the $Cu_3(BTC)_2$&GO mixture was simply mixed with preformed $Cu_3(BTC)_2$ (94 wt %) and GO (6 wt %). For the later, H_3BTC (0.06 g) was dissolved in 5 mL of DMF solution, and $Cu(NO_3)_2$ (0.06 g) was dissolved in deionized water (10 mL), respectively. Then two solutions together with a GO aqueous suspension (5 mL) were mixed and stirred at 85 °C for 6 h. The mixture was then filtered, washed, and dried. Finally, a $Cu_3(BTC)_2$&GO hybrid product was obtained."

Characterizations. The morphology of the samples was characterized by optical micrography on a Nikon A1R. Field-emission scanning electron microscope (FESEM) images were taken by using a Nova NanoSEM 450. Powder X-ray diffraction (PXRD) patterns were recorded on a D/Max2550 VB/PC spectrometer using Cu Kα radiation (40 kV and 200 mA). Fourier transform infrared (FTIR) spectra of the samples were recorded at room temperature on a Thermo Scientific Nicolet iS10. Nitrogen adsorption measurements were conducted at 77.4 K on a Micrometrics ASAP 2020 sorption meter. The total surface area was determined by the Brunauer−Emmett−Teller (BET) model. Thermogravimetric analysis (TG) measurements were performed on a Netzsch STA 449 F3 Jupiter. Mass spectrometry (MS) measurements were conducted on a Netzsch QMS 403 D Aëolos.

Gas Adsorption Measurements. CO_2 adsorption capacities of the samples were determined by a Micrometrics ASAP 2020 at 25 °C, and all samples were degassed for 12 h at 120 °C under vacuum before the measurement. To examine the CO_2 adsorption of the obtained $Cu_3(BTC)_2$/GO composites in the presence of water, we proposed a practical quantitative method through the joint TG-MS. The samples were first degassed in a pure N_2 stream with a flow rate of 20 mL/min at 120 °C for 5 h in the oven of the thermogravimetric analyzer. After cooling to 25 °C, the samples were exposed to a simulated flue gas in which 50% relative humidity was introduced into the gas mixture of CO_2 and N_2 at a fixed ratio of 15:85 CO_2/N_2 (v/v). Adsorption took place under the humid CO_2/N_2 mixture feed stream. The flow rate of the whole feed stream was 20 mL/min. Purge desorption for 120 min followed by thermal desorption at up to 200 °C with a heating rate of 5 °C/min was carried out under pure N_2 with a flow rate of 20 mL/min. The signals of the mass loss of the samples as well as the mass spectrometry of H_2O (mass/charge ratio = 18) were recorded simultaneously during the desorption process. For the calculation of the adsorption capacities of H_2O and CO_2, a calibration experiment was conducted in which 5 Å zeolite was exposed to a humid N_2 feed stream (50% relative humidity but without CO_2) for the adsorption while the following thermal desorption process and other conditions remained the same.

RESULTS AND DISCUSSION

As illustrated in Scheme 1, with the precursors of $Cu_3(BTC)_2$ of H_3BTC ligands dissolved in the *n*-octanol phase and $Cu(NO_3)_2$ in the water phase, the *n*-octanol/water emulsion system is stabilized by GO sheets. All droplets of the GO Pickering emulsions (Figure S1a) show a smooth interface and a relatively homogeneous size distribution. The size of GO sheets is likely to greatly affect the stability and quality of the Pickering emulsion formed. The large GO sheets (>5 μm) are less hydrophilic so that they can float on the water surface whereas small (<1 μm), more hydrophilic GO sheets sink into the subphase.[33−35] Because most GO sheets produced in this work were large (Figure S1b), it ensured the good stability of the Pickering emulsion of the *n*-octanol/water system and provided a large interfacial area for the interfacial growth of $Cu_3(BTC)_2$ nanoparticles. We proposed the mechanism of the interfacial growth of $Cu_3(BTC)_2$ as that inside the GO Pickering emulsions, and H_3BTC would diffuse toward the GO surface driven by the concentration gradient while Cu^{2+} ions would be adsorbed at the GO surface via the electrostatic interaction and the coordination with oxygen-containing functional groups. As a result, the interfacial nucleation of the $Cu_3(BTC)_2$ nanoparticle could easily take place at the surface of GO sheets, which float stably at the *n*-octanol/water interface, to produce a $Cu_3(BTC)_2$/GO composite. This proposed mechanism was confirmed by the optical and polarized optical micrographs of obtained $Cu_3(BTC)_2$/GO composites. As shown in Figure 1, covered with many particles, the surfaces of all of the GO emulsion droplets become coarse, which gives clear evidence of the growth of $Cu_3(BTC)_2$ nanoparticles at the surface of the GO emulsion droplets. The polarized optical micrographs show more intuitively that the emulsion droplets are covered by the column-like or granular-like $Cu_3(BTC)_2$ nanocrystals. When the added amount of GO is increased, the diameter of the emulsion droplets decreases from 50 μm for $Cu_3(BTC)_2$/GO-l to about 40 μm for $Cu_3(BTC)_2$/GO-h. Accordingly, the total interfacial area increases, resulting in denser coverage of the $Cu_3(BTC)_2$ crystals. After storage for 1 week (Figure S2b), the $Cu_3(BTC)_2$/GO-m emulsion system exhibits little deterioration compared to its fresh counterpart (Figure S2a). Even after a
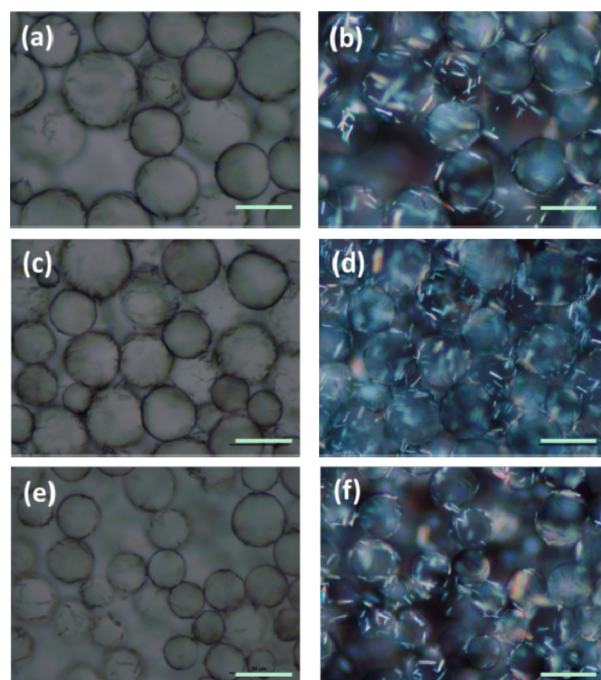
Figure 1. Optical micrographs and polarized optical micrographs of $Cu_3(BTC)_2$/GO-l (a, b), $Cu_3(BTC)_2$/GO-m (c, d), and $Cu_3(BTC)_2$/GO-h (e, f). The scale bar in each image is 50 μm.

secondary emulsification under high shearing forces at a speed of 10 000 rpm for 5 min, the emulsion system (Figure S2c) is still stable.

TEM images (Figure 2) of $Cu_3(BTC)_2$/GO-m powder after drying as well as $Cu_3(BTC)_2$/GO-l and $Cu_3(BTC)_2$/GO-h
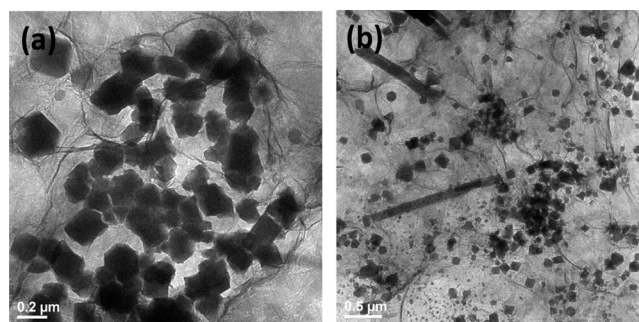

Figure 2. TEM images of the $Cu_3(BTC)_2$/GO-m composite.

powders (Figure S3) further reveal that most of the $Cu_3(BTC)_2$ nanocrystals are regular octahedrons with an average size of about 100−200 nm, while some of them developed into a columnar rod with a length of 1 to 2 μm, consistent with the morphology observed by the polar micrographs. However, the granular-like $Cu_3(BTC)_2$ nanocrystals were too small to be observed in the micrographs. Because of the spatial restriction of GO sheets, $Cu_3(BTC)_2$ crystals can grow up only in one direction, resulting in a columnar rod rather than a large 3D octahedron at the GO surface. The in situ growth of $Cu_3(BTC)_2$ crystals was further confirmed by the FTIR spectra and the PXRD patterns. All of the characteristic peaks of pristine $Cu_3(BTC)_2$ crystals can be found on the FTIR spectra of $Cu_3(BTC)_2$/GO composites (Figure S4a), such as the bands in the region of 700−1300 cm^{-1} assigned to the fingerprint region and the out-of-plane vibrations of BTC; the bands at
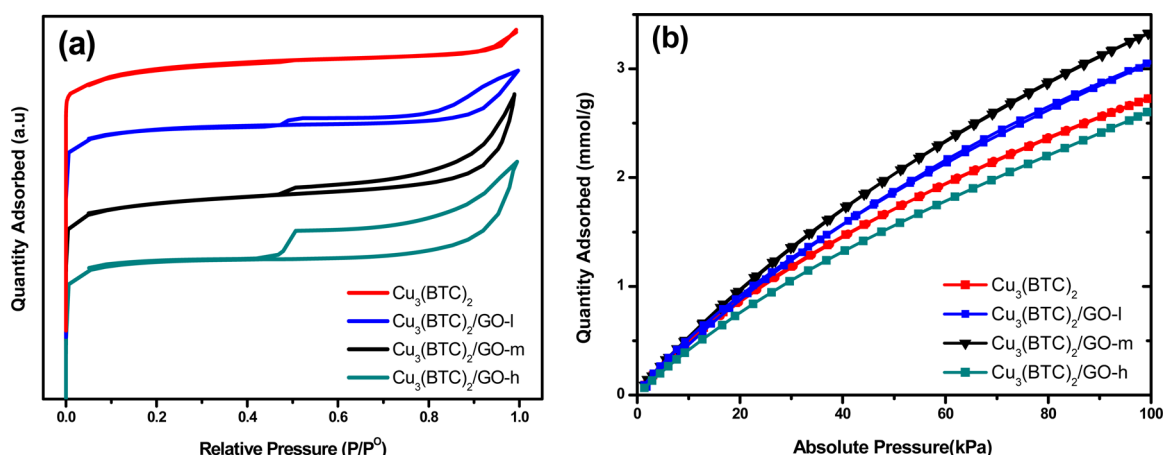
Figure 3. (a) N_2 adsorption isotherms collected at 77 K. (b) CO_2 adsorption isotherms collected at 298 K for each $Cu_3(BTC)_2$/GO composite powder after drying.
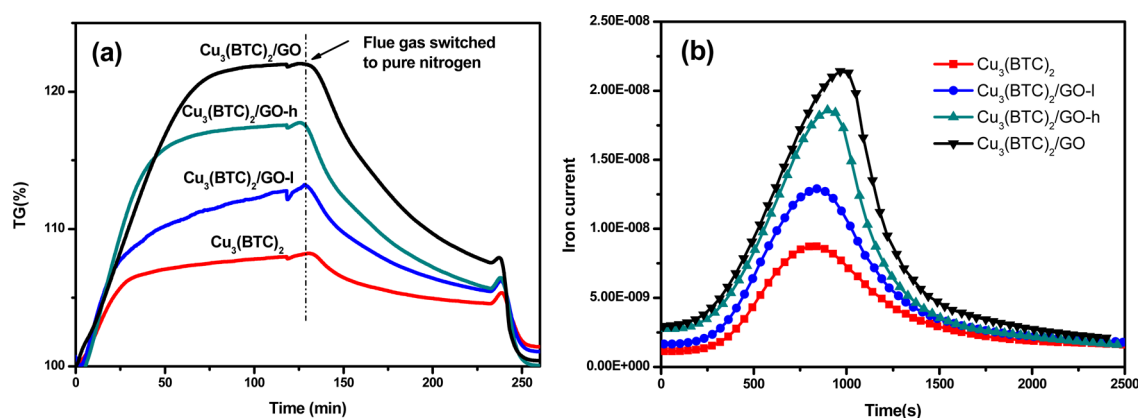
Figure 4. (a) TG curves of dynamic adsorption−desorption and (b) MS curves of H_2O during desorption on each $Cu_3(BTC)_2$/GO composite.

1380 cm^{-1} are due to the symmetric stretching of carboxylic groups, and those at 1560, 1650, and 1675 cm^{-1} are attributed to the asymmetric stretching of carboxylic groups in BTC as well as the C=O stretch of the carboxylate group located on the surface of GO, confirming the successful growth of $Cu_3(BTC)_2$ nanoparticles on GO sheets. Similarly, because $Cu_3(BTC)_2$ is the major component of $Cu_3(BTC)_2$/GO composites, their XRD patterns (Figure S4b) also clearly present characteristic features of the pristine $Cu_3(BTC)_2$ as expected. More importantly, from the TEM images, we can see that GO sheets, as the stabilizer of the Pickering emulsion, are well exfoliated and highly extended even after the interfacial growth of $Cu_3(BTC)_2$ nanoparticles. The unique structure of the composites of small $Cu_3(BTC)_2$ nanocrystals highly dispersed at the surface of the exfoliated GO sheets would lead to more active adsorption sites exposed and would decrease the length for the gas molecules transferring, which are highly in favor of improving its CO_2 adsorption performance in both thermodynamic and dynamic ways.

N_2 adsorption−desorption isotherms of $Cu_3(BTC)_2$/GO composites at 77 K (Figure 3) show a typical type I adsorption isotherm, and the steep rise in the amount of N_2 adsorbed in the low-pressure region suggests the presence of a large portion of micropores in each $Cu_3(BTC)_2$/GO composite. A hysteresis loop is also observed with increasing relative pressure $p/p°$ close to 1, indicating the presence of mesopores or macropores caused by the close packing of $Cu_3(BTC)_2$ nanocrystals at the

surface of GO sheets or the aggregation of $Cu_3(BTC)_2$/GO composite particles. The hysteresis loop is broadened upon increasing the added amount of GO, indicating that the structure is dependent on the GO content. As summarized in Table S1, the BET surface area is present in the decreasing sequence 933, 898, 837, and 743 m^2 g^{-1} for pure $Cu_3(BTC)_2$, $Cu_3(BTC)_2$/GO-l, $Cu_3(BTC)_2$/GO-m, and $Cu_3(BTC)_2$/GO-h, respectively, because GO makes no contribution to the surface area and the larger the added amount of GO, the smaller the surface area. However, $Cu_3(BTC)_2$/GO composites exhibit a much higher volume compared to pure $Cu_3(BTC)_2$, which might be caused by the distortion of the first layer of $Cu_3(BTC)_2$ structure developed at the surface of GO sheets.[44] As the GO content increases, the maximum pore volume reaches as high as 0.19 cm^3 g^{-1} for $Cu_3(BTC)_2$/GO-m. However, too large a GO content results in a denser formation of the $Cu_3(BTC)_2$ nanocrystals in the composites, and the volume would not increase further.

Pure CO_2 adsorption isotherms are collected at 298 K on each $Cu_3(BTC)_2$/GO composite to investigate their CO_2 adsorption capacity (Figure 3b). Compared to pure $Cu_3(BTC)_2$, the CO_2 adsorption capacity increases significantly from 2.77 to 3.13 and 3.37 mmol/g for $Cu_3(BTC)_2$/GO-l and $Cu_3(BTC)_2$/GO-m, respectively, but decreases to 2.66 mmol/g for $Cu_3(BTC)_2$/GO-h. With suitable GO added, it can significantly modify the morphology and surface porosity of $Cu_3(BTC)_2$ nanoparticles and hence increase the CO_2

adsorption, respectively.[45,46] Determined by TG analysis (Figure S5, including the calculation details), the $Cu_3(BTC)_2$ contents in $Cu_3(BTC)_2$/GO-l, $Cu_3(BTC)_2$/GO-m, and $Cu_3(BTC)_2$/GO-h composites are about 95.12, 93.90, and 92.77 wt %, respectively. Too much added GO resulted in a small percentage of $Cu_3(BTC)_2$ in the $Cu_3(BTC)_2$/GO-h composite and a small CO_2 adsorption capacity because GO itself makes only a small contribution to the CO_2 adsorption capacity.

For the real CO_2 capture from the postcombustion flue gas, the influence of water could not be ignored.[47−49] In our previous work, we developed a convenient quantitative method through TG-MS to determine the dynamic CO_2 uptake from the simulated flue gas in the presence of water.[50] Because the affinity of CO_2 and H_2O are much stronger than that of N_2 on $Cu_3(BTC)_2$, the weight increase (or loss) during the adsorption (or desorption) process is supposed to be attributed only to the adsorption (or desorption) of CO_2 and H_2O. Meanwhile, MS was used to monitor the amount of desorbed H_2O in the effluent during the desorption process. The peak area of H_2O in the MS curve is proportional to the amount of H_2O adsorbed in the sample, and the proportionality coefficient R_{H_2O} (the ratio of mass/area) was determined to be 2.523. On this basis, H_2O uptake from the simulated flue gas for any sample can be calculated by multiplying the peak area in its corresponding H_2O MS curve by R_{H_2O}. CO_2 uptake can then be estimated by subtracting the calculated amount of H_2O from the total mass increase in the TG curve determined during the adsorption process.

Figure 4a shows the dynamic adsorption and desorption curves determined by TG when the samples were exposed to the simulated flue gas containing 15% (v/v) CO_2 in N_2 with 50% relative humidity for 120 min before experiencing thermal desorption under purging with pure N_2. Meanwhile, the amounts of H_2O desorbed in the effluent during the desorption process were monitored by their MS curves (Figure 4b). The H_2O and CO_2 uptakes of all samples were measured and calculated (Table S2). The final results are summarized in Table 1. All $Cu_3(BTC)_2$/GO composites show significantly improved CO_2 uptake and CO_2/H_2O selectivity under the humid condition compared to pristine $Cu_3(BTC)_2$ as well as

GO, indicating the successful designing methodology of $Cu_3(BTC)_2$/GO composite adsorbent.

As listed in Table 1, the CO_2 adsorption capacity of pristine $Cu_3(BTC)_2$ from dry and pure CO_2 is 2.77 mmol/g, but when it was exposed to the simulated flue gas in the presence of humidity for 120 min, the dynamic CO_2 uptake decreased significantly to 0.64 mmol/g. This is because the microporous $Cu_3(BTC)_2$ has a better affinity for the polar H_2O molecule (3.57 mmol/g) than for the CO_2 molecule, the preoccupied H_2O molecules exclusively form CO_2 molecules from adsorption, and even worse, H_2O molecules might attack MOF metal clusters and destroy the MOF skeleton structure to some degree.[7] Whereas for the pristine GO, with the basal planes of the carbon networks and the oxygen-containing functional groups, it shows a great affinity for H_2O molecules and H_2O uptake is as high as 7.20 mmol/g. When two components assemble together to produce $Cu_3(BTC)_2$/GO composites through the Pickering emulsion, the CO_2 adsorption performance will be significantly improved. For $Cu_3(BTC)_2$/GO-m under the same dynamic adsorption conditions, its CO_2 uptake from the simulated flue gas with 15% CO_2 in the presence of humidity could be maintained as high as 3.19 mmol/g, with only a little lower than the equilibrium CO_2 adsorption capacity of 3.37 mmol/g from the dry and pure CO_2 flow. Because of the unique structure of $Cu_3(BTC)_2$/GO composites in which $Cu_3(BTC)_2$ nanocrystals were evenly distributed on the surface of highly exfoliated GO sheets, most H_2O molecules would be predominantly adsorbed on GO sheets (7.15 mmol/g), which significantly decrease their occupancy in the pores of $Cu_3(BTC)_2$ nanocrystals. As a result, CO_2 uptake in $Cu_3(BTC)_2$ is maintained at a high level, and both CO_2 and H_2O uptakes are high. For $Cu_3(BTC)_2$/GO-l, when the added amount of GO is not large enough, CO_2 uptake from the simulated flue gas still shows a significant decrease compared to its CO_2 capacity under dry conditions, although it is already much better than that of the pristine $Cu_3(BTC)_2$. On the contrary, for $Cu_3(BTC)_2$/GO-h, more added GO would improve the water resistance and degrade CO_2 uptake as well. Because the surface area of $Cu_3(BTC)_2$/GO-h shows a significant decrease, both CO_2 and H_2O uptakes are lower than that of $Cu_3(BTC)_2$/GO-m. These phenomena indicate that GO can effectively adsorb H_2O molecules but allow the free diffusion of CO_2 molecules into $Cu_3(BTC)_2$ nanocrystals, maintaining the overall good CO_2 uptake even in the presence of humidity for 120 min.

Meanwhile, when we make an enlargement of the initial segments of dynamic adsorption curves (Figure S6), we can see that the adsorption rate is in the sequence of $Cu_3(BTC)_2$/GO-h > $Cu_3(BTC)_2$/GO-m > $Cu_3(BTC)_2$/GO-l > $Cu_3(BTC)_2$, indicating that with increased amounts of GO, the total initial adsorption rate increases. To understand clearly which component between CO_2 and H_2O is the dominant contribution for the overall initial uptakes, we took $Cu_3(BTC)_2$/GO-m as an example to investigate the changes in CO_2 and H_2O uptakes with the adsorption time (Table S3). As shown in Figure 5, the H_2O adsorption rate is much faster than CO_2. At 30 min, H_2O uptake is as high as 4.95 mmol/g, whereas CO_2 uptake is only 1.64 mmol/g. Because GO is responsive for the adsorption of H_2O, $Cu_3(BTC)_2$/GO-h, with the largest added amount of GO, shows the fastest initial adsorption rate. After that, CO_2 uptake keeps increasing whereas the increase of H_2O uptake slows down. At 60 min, CO_2 uptake is 3.30 mmol/g, almost the same as the adsorption

**Table 1. Dynamic Adsorption on $Cu_3(BTC)_2$, GO, and $Cu_3(BTC)_2$/GO Composites from the Simulated Flue Gas in the Presence of Humidity and Comparison with the Equilibrium CO_2 Adsorption Capacity**

sample	GO content [%]	CO_2 capacity, dry [mmol g^{-1}]^a	CO_2 uptake, wet [mmol g^{-1}]^b	H_2O uptake [mmol g^{-1}]^c
$Cu_3(BTC)_2$	0	2.77	0.64	3.57
$Cu_3(BTC)_2$/GO-l	4.88	3.13	1.57	5.61
$Cu_3(BTC)_2$/GO-m	6.06	3.37	3.19	7.15
$Cu_3(BTC)_2$/GO-h	7.23	2.66	2.20	5.96
GO	100		0.91	7.20

^{a}Determined by the equilibrium pure CO_2 adsorption isotherm at 298 K, 1 bar. ^{b}Determined by the total amount of dynamic adsorption minus the amount of H_2O uptake when exposing the adsorbent in the simulated flue gas in the presence of humidity for 120 min. ^{c}Determined by the area of the H_2O MS peak multiplying R_{H_2O}.
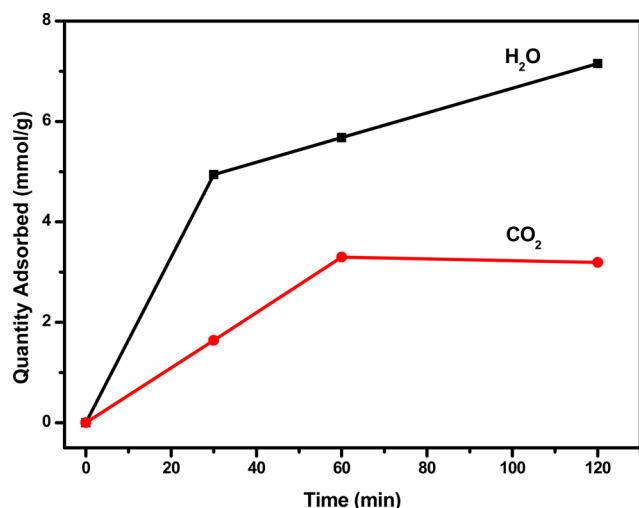
Figure 5. Changes in CO_2 and H_2O uptakes with adsorption time on $Cu_3(BTC)_2$/GO-m from the simulated flue gas in the presence of humidity.

capacity from dry and pure CO_2, suggesting that with GO protection, H_2O almost shows no negative effect on CO_2 adsorption. Even for prolonged adsorption to 120 min, although the H_2O uptake keeps on increasing to 7.15 mmol/g, the CO_2 uptake can maintain a high value of 3.30 mmol/g. Usually, 120 min is long enough for a real adsorption and separation process, Therefore, the water-resistant ability of $Cu_3(BTC)_2$/GO composites would be very meaningful for real CO_2 capture in the future.

Compared to the $Cu_3(BTC)_2$&GO hybrid by growing $Cu_3(BTC)_2$ in the bulk GO aqueous suspension without emulsification or the $Cu_3(BTC)_2$&GO mixture by simply mixing, $Cu_3(BTC)_2$/GO composites show a significantly improved CO_2 capacity under the humid condition, indicating the successful design and preparation methodology of the in situ interfacial growth. As listed in Table S4 and shown in Figure S7, the CO_2 uptake of $Cu_3(BTC)_2$/GO-m could be as high as 3.30 mmol/g at high humidity for 60 min, whereas the $Cu_3(BTC)_2$&GO hybrid and $Cu_3(BTC)_2$&GO mixture are only 1.56 and 1.27 mmol/g under the same testing conditions. In the samples of the $Cu_3(BTC)_2$&GO hybrid and $Cu_3(BTC)_2$&GO mixture, GO sheets could not be as highly exfoliated and extended as those in the $Cu_3(BTC)_2$/GO composite. It appears that highly extended GO sheets on the surface of the $Cu_3(BTC)_2$/GO composite are acting as a "sponge" for the water vapor present in the gas flow, enabling the MOF to absorb CO_2. Therefore, the synergistic effect of the nanocomposites synthesized via the in situ interfacial synthesis approach induced by the Pickering emulsion is very interesting and attractive.

CONCLUSIONS

A novel in situ interfacial growth of nanoparticles induced by the Pickering emulsion strategy was proposed for the fabrication of MOF/GO composites. The GO sheet is a promising stabilizer for the Pickering emulsion and hence provides a large interfacial area for the interfacial growth of $Cu_3(BTC)_2$ nanoparticles. The well-exfoliated and extended GO sheets in the obtained $Cu_3(BTC)_2$/GO composites showed a great affinity for H_2O molecules and significantly reduced their occupation in $Cu_3(BTC)_2$ nanoparticles. There-

fore, with a suitable amount of GO incorporated, $Cu_3(BTC)_2$/GO-m exhibited good CO_2 adsorption. From the simulated flue gas at high humidity, CO_2 uptake of $Cu_3(BTC)_2$/GO-m was as high as 3.30 mmol g^{-1} and remainted this high for about 120 min. The efficient CO_2 capture in both thermodynamic and dynamic ways highlighted the potential application of $Cu_3(BTC)_2$/GO composites. More importantly, this in situ interfacial growth of nanoparticles induced by the Pickering emulsion strategy provided a convenient and general method for the fabrication of various task-specific nanocomposites.

ASSOCIATED CONTENT

Ⓢ Supporting Information

Optical micrograph and polarized optical micrograph of a GO Pickering emulsion. FTIR spectra, PXRD patterns, TG curves, dynamic adsorption curves, porosity, and dynamic CO_2 and H_2O uptake on $Cu_3(BTC)_2$/GO composites. The Supporting Information is available free of charge on the ACS Publications website at DOI: 10.1021/acs.langmuir.5b01171.

AUTHOR INFORMATION

Corresponding Author

*E-mail: junhu@ecust.edu.cn.

Author Contributions

The manuscript was written through the contributions of all authors. All authors have given approval to the final version of the manuscript.

Notes

The authors declare no competing financial interest.

ACKNOWLEDGMENTS

REFERENCES

(1) Aaron, D.; Tsouris, C. Separation of CO_2 from Flue Gas: A Review. *Sep. Sci. Technol.* **2005**, *40*, 321−348.

(2) Chaffee, A.; Knowles, G.; Liang, Z.; Zhang, J.; Xiao, P.; Webley, P. CO_2 capture by adsorption: Materials and process development. *Int. J. Greenhouse Gas Control* **2007**, *1*, 11−18.

(3) Zhang, Z.; Yao, Z.-Z.; Xiang, S.; Chen, B. Perspective of microporous metal−organic frameworks for CO_2 capture and separation. *Energy Environ. Sci.* **2014**, *7*, 2868−2899.

(4) Hudson, M. R.; Queen, W. L.; Mason, J. A.; Fickel, D. W.; Lobo, R. F.; Brown, C. M. Unconventional, highly selective CO_2 adsorption in zeolite SSZ-13. *J. Am. Chem. Soc.* **2012**, *134*, 1970−1973.

(5) Aijaz, A.; Akita, T.; Yang, H.; Xu, Q. From ionic-liquid@metal-organic framework composites to heteroatom-decorated large-surface area carbons: superior CO_2 and H_2 uptake. *Chem. Commun.* **2014**, *50*, 6498−6501.

(6) Zhu, Q. L.; Xu, Q. Metal-organic framework composites. *Chem. Soc. Rev.* **2014**, *43*, 5468−5512.

(7) Kaye, S. S.; Dailly, A.; Yaghi, O. M.; Long, J. R. Impact of Preparation and Handling on the Hydrogen Storage Properties of Zn_4O(1,4-benzenedicarboxylate)$_3$ (MOF-5). *J. Am. Chem. Soc.* **2007**, *129*, 14176−14177.

(8) Low, J. J.; Benin, A. I.; Jakubczak, P.; Abrahamian, J. F.; Faheem, S. A.; Willis, R. R. Virtual High Throughput Screening Confirmed

Experimentally: Porous Coordination Polymer Hydration. *J. Am. Chem. Soc.* **2009**, *131*, 15834−15842.

(9) Nugent, P.; Belmabkhout, Y.; Burd, S. D.; Cairns, A. J.; Luebke, R.; Forrest, K.; Pham, T.; Ma, S.; Space, B.; Wojtas, L.; Eddaoudi, M.; Zaworotko, M. J. Porous materials with optimal adsorption thermodynamics and kinetics for CO_2 separation. *Nature* **2013**, *495*, 80−84.

(10) Li, G.; Xiao, P.; Webley, P.; Zhang, J.; Singh, R.; Marshall, M. Capture of CO_2 from high humidity flue gas by vacuum swing adsorption with zeolite 13X. *Adsorption* **2008**, *14*, 415−422.

(11) Chaemchuen, S.; Kabir, N. A.; Zhou, K.; Verpoort, F. Metal-organic frameworks for upgrading biogas via CO_2 adsorption to biogas green energy. *Chem. Soc. Rev.* **2013**, *42*, 9304−9332.

(12) Cheng, P.; Hu, Y. H. H2O-Functionalized Zeolitic Zn(2-methylimidazole)$_2$Framework (ZIF-8) for H2Storage. *J. Phys. Chem. C* **2014**, *118*, 21866−21872.

(13) Zhang, W.; Hu, Y.; Ge, J.; Jiang, H. L.; Yu, S. H. A facile and general coating approach to moisture/water-resistant metal-organic frameworks with intact porosity. *J. Am. Chem. Soc.* **2014**, *136*, 16978−16981.

(14) Liu, Y.; Ng, Z.; Khan, E. A.; Jeong, H.-K.; Ching, C.-b.; Lai, Z. Synthesis of continuous MOF-5 membranes on porous α-alumina substrates. *Microporous Mesoporous Mater.* **2009**, *118*, 296−301.

(15) Li, Z.; Zeng, H. C. Armored MOFs: Enforcing Soft Microporous MOF Nanocrystals with Hard Mesoporous Silica. *J. Am. Chem. Soc.* **2014**, *136*, 5631−5639.

(16) Huang, A. S.; Caro, J. Covalent Post-Functionalization of Zeolitic Imidazolate Framework ZIF-90 Membrane for Enhanced Hydrogen Selectivity. *Angew. Chem., Int. Ed.* **2011**, *50*, 4979−4982.

(17) Arslan, H. K.; Shekhah, O.; Wieland, D. C.; Paulus, M.; Sternemann, C.; Schroer, M. A.; Tiemeyer, S.; Tolan, M.; Fischer, R. A.; Woll, C. Intercalation in layered metal-organic frameworks: reversible inclusion of an extended pi-system. *J. Am. Chem. Soc.* **2011**, *133*, 8158−8161.

(18) Petit, C.; Mendoza, B.; O'Donnell, D.; Bandosz, T. J. Effect of graphite features on the properties of metal-organic framework/graphite hybrid materials prepared using an in situ process. *Langmuir* **2011**, *27*, 10234−10242.

(19) Rodenas, T.; Luz, I.; Prieto, G.; Seoane, B.; Miro, H.; Corma, A.; Kapteijn, F.; Llabres i Xamena, F. X.; Gascon, J. Metal-organic framework nanosheets in polymer composite materials for gas separation. *Nat. Mater.* **2015**, *14*, 48−55.

(20) Prasanth, K. P.; Rallapalli, P.; Raj, M. C.; Bajaj, H. C.; Jasra, R. V. Enhanced hydrogen sorption in single walled carbon nanotube incorporated MIL-101 composite metal−organic framework. *Int. J. Hydrogen Energy* **2011**, *36*, 7594−7601.

(21) Bashkova, S.; Bandosz, T. J. Insight into the role of the oxidized graphite precursor on the properties of copper-based MOF/graphite oxide composites. *Microporous Mesoporous Mater.* **2013**, *179*, 205−211.

(22) Policicchio, A.; Zhao, Y.; Zhong, Q.; Agostino, R. G.; Bandosz, T. J. Cu-BTC/Aminated Graphite Oxide Composites As High-Efficiency CO_2 Capture Media. *ACS Appl. Mater. Interfaces* **2013**, *6*, 101−108.

(23) Patel, D. G.; Walton, I. M.; Cox, J. M.; Gleason, C. J.; Butzer, D. R.; Benedict, J. B. Photoresponsive porous materials: the design and synthesis of photochromic diarylethene-based linkers and a metal-organic framework. *Chem. Commun.* **2014**, *50*, 2653−2656.

(24) Zhu, P.; Sumpter, B. G.; Meunier, V. Electronic, Thermal, and Structural Properties of Graphene Oxide Frameworks. *J. Phys. Chem. C* **2013**, *117*, 8276−8281.

(25) Huang, A.; Liu, Q.; Wang, N.; Zhu, Y.; Caro, J. Bicontinuous zeolitic imidazolate framework ZIF-8@GO membrane with enhanced hydrogen selectivity. *J. Am. Chem. Soc.* **2014**, *136*, 14686−14689.

(26) Petit, C.; Bandosz, T. J. Synthesis, Characterization, and Ammonia Adsorption Properties of Mesoporous Metal-Organic Framework (MIL(Fe))-Graphite Oxide Composites: Exploring the Limits of Materials Fabrication. *Adv. Funct. Mater.* **2011**, *21*, 2108−2117.

(27) Zhao, Y.; Seredych, M.; Zhong, Q.; Bandosz, T. J. Superior performance of copper based MOF and aminated graphite oxide composites as CO_2 adsorbents at room temperature. *ACS Appl. Mater. Interfaces* **2013**, *5*, 4951−4959.

(28) Bian, Z.; Zhu, X.; Jin, T.; Gao, J.; Hu, J.; Liu, H. Ionic liquid-assisted growth of $Cu_3(BTC)_2$ nanocrystals on graphene oxide sheets: Towards both high capacity and high rate for CO_2 adsorption. *Microporous Mesoporous Mater.* **2014**, *200*, 159−164.

(29) Levasseur, B.; Petit, C.; Bandosz, T. J. Reactive adsorption of NO2 on copper-based metal-organic framework and graphite oxide/metal-organic framework composites. *ACS Appl. Mater. Interfaces* **2010**, *2*, 3606−3613.

(30) Hernandez, Y.; Nicolosi, V.; Lotya, M.; Blighe, F. M.; Sun, Z.; De, S.; McGovern, I. T.; Holland, B.; Byrne, M.; Gun'Ko, Y. K.; Boland, J. J.; Niraj, P.; Duesberg, G.; Krishnamurthy, S.; Goodhue, R.; Hutchison, J.; Scardaci, V.; Ferrari, A. C.; Coleman, J. N. High-yield production of graphene by liquid-phase exfoliation of graphite. *Nat. Nano* **2008**, *3*, 563−568.

(31) Wang, H.; Sun, K.; Tao, F.; Stacchiola, D. J.; Hu, Y. H. 3D honeycomb-like structured graphene and its high efficiency as a counter-electrode catalyst for dye-sensitized solar cells. *Angew. Chem.* **2013**, *52*, 9210−9214.

(32) Sun, Z.; Feng, T.; Russell, T. P. Assembly of graphene oxide at water/oil interfaces: tessellated nanotiles. *Langmuir* **2013**, *29*, 13407−13413.

(33) Jaemyung Kim, L. J. C.; Kim, F.; Yuan, W.; Shull, K. R.; Huang, J. Graphene Oxide Sheets at Interfaces. *J. Am. Chem. Soc.* **2010**, *132*, 8180−8186.

(34) Jiayan Luo, L. J. C.; Tung, V. C.; Tan, A. T. L.; Goins, P. E.; Wu, J.; Huang, J.; Huang, J. Graphene Oxide Nanocolloids. *J. Am. Chem. Soc.* **2010**, *132*, 17667−17669.

(35) Cote, L. J.; Kim, J.; Tung, V. C.; Luo, J.; Kim, F.; Huang, J. Graphene oxide as surfactant sheets. *Pure Appl. Chem.* **2010**, *83*, 95−110.

(36) Thomassin, J.-M.; Trifkovic, M.; Alkarmo, W.; Detrembleur, C.; Jérôme, C.; Macosko, C. Poly(methyl methacrylate)/Graphene Oxide Nanocomposites by a Precipitation Polymerization Process and Their Dielectric and Rheological Characterization. *Macromolecules* **2014**, *47*, 2149−2155.

(37) Shao, J. J.; Lv, W.; Yang, Q. H. Self-assembly of graphene oxide at interfaces. *Adv. Mater.* **2014**, *26*, 5586−5612.

(38) Nypelo, T.; Rodriguez-Abreu, C.; Kolen'ko, Y. V.; Rivas, J.; Rojas, O. J. Microbeads and hollow microcapsules obtained by self-assembly of pickering magneto-responsive cellulose nanocrystals. *ACS Appl. Mater. Interfaces* **2014**, *6*, 16851−16858.

(39) He, Y.; Wu, F.; Sun, X.; Li, R.; Guo, Y.; Li, C.; Zhang, L.; Xing, F.; Wang, W.; Gao, J. Factors that affect Pickering emulsions stabilized by graphene oxide. *ACS Appl. Mater. Interfaces* **2013**, *5*, 4843−4855.

(40) Zhang, M.; Ngo, T. H.; Rabiah, N. I.; Otanicar, T. P.; Phelan, P. E.; Swaminathan, R.; Dai, L. L. Core-shell and asymmetric polystyrene-gold composite particles via one-step Pickering emulsion polymerization. *Langmuir* **2014**, *30*, 75−82.

(41) Gudarzi, M. M.; Sharif, F. Self assembly of graphene oxide at the liquid-liquid interface: A new route to the fabrication of graphene based composites. *Soft Matter* **2011**, *7*, 3432−3440.

(42) Tang, M.; Wang, X.; Wu, F.; Liu, Y.; Zhang, S.; Pang, X.; Li, X.; Qiu, H. Au nanoparticle/graphene oxide hybrids as stabilizers for Pickering emulsions and Au nanoparticle/graphene oxide@polystyrene microspheres. *Carbon* **2014**, *71*, 238−248.

(43) Hummers, W. S.; Offeman, R. E. *J. Am. Chem. Soc.* **1958**, *80*, 1339−1339.

(44) Huang, Z. H.; Liu, G.; Kang, F. Glucose-promoted Zn-based metal-organic framework/graphene oxide composites for hydrogen sulfide removal. *ACS Appl. Mater. Interfaces* **2012**, *4*, 4942−4947.

(45) Petit, C.; Bandosz, T. J. Enhanced Adsorption of Ammonia on Metal-Organic Framework/Graphite Oxide Composites: Analysis of Surface Interactions. *Adv. Funct. Mater.* **2010**, *20*, 111−118.

(46) Petit, C.; Mendoza, B.; Bandosz, T. J. Reactive adsorption of ammonia on Cu-based MOF/graphene composites. *Langmuir* **2010**, *26*, 15302−15309.

(47) Li, D.; Furukawa, H.; Deng, H.; Liu, C.; Yaghi, O. M.; Eisenberg, D. S. Designed amyloid fibers as materials for selective carbon dioxide capture. *Proc. Natl. Acad. Sci. U.S.A.* **2014**, *111*, 191−196.

(48) Fracaroli, A. M.; Furukawa, H.; Suzuki, M.; Dodd, M.; Okajima, S.; Gandara, F.; Reimer, J. A.; Yaghi, O. M. Metal-organic frameworks with precisely designed interior for carbon dioxide capture in the presence of water. *J. Am. Chem. Soc.* **2014**, *136*, 8863−8866.

(49) Shekhah, O.; Belmabkhout, Y.; Chen, Z.; Guillerm, V.; Cairns, A.; Adil, K.; Eddaoudi, M. Made-to-order metal-organic frameworks for trace carbon dioxide removal and air capture. *Nat. Commun.* **2014**, *5*, 4228−4235.

(50) Gao, F.; Li, Y.; Bian, Z.; Hu, J.; Liu, H. Dynamic Hydrophobic Hindrance Effect of Zeolite@Zeolitic Imidazolate Framework Composites for CO_2 Capture in the Presence of Water. *J. Mater. Chem. A* **2015**, *3*, 8091−8097.